RESEARCH ARTICLE

National Science Review
0: nwag489, 2026
https://doi.org/10.1093/nsr/nwag489
Advance access publication 19 August 2026

MATERIALS SCIENCE

Self-n-doped small molecules for highly stable and low-power biosensing

Xun Lei [1,†], Yuqiu Lei [2,†], Kai-Kai Liu [1,†], Peiyun Li [1,*], Xin-Yu Deng [1], Gaoyang Ge [1], Jingyi Wang [1], Maria A. Komkova [3], Zhi Zhang [1,*] and Ting Lei [1,*]

ABSTRACT

Minimizing power consumption and improving long-term stability of bioelectronic devices are crucial for ensuring prolonged operation and reducing the risk of tissue damage. Organic electrochemical transistors (OECTs) have gained widespread attention in biosensing applications due to their high transconductance and excellent biocompatibility. Although considerable efforts have been directed toward optimizing performance metrics (e.g. μC^*) in OECTs, strategies to reduce power consumption have been largely overlooked, despite their critical importance for large-scale integration and *in vivo* sensing applications. Here, we present a unique self-doping strategy to achieve low power consumption in OECTs. Small molecules with certain end groups can undergo self-doping through ethylene glycol side chains, enabling n-type depletion-mode OECTs with near-zero threshold voltage (V_{Th}) and outstanding long-term stability. Based on these findings, we developed biosensors with high signal-to-noise ratios while operating at an ultra-low power consumption of 12 nW. Our findings highlight self-doping molecules for energy-efficient biosensing.

Keywords: n-type small molecules, self-doping, organic electrochemical transistors, low-power sensing

[1]National Key Laboratory of Advanced Micro and Nano Manufacture Technology, Key Laboratory of Polymer Chemistry and Physics of Ministry of Education, School of Materials Science and Engineering, Peking University, Beijing 100871, China; [2]College of Engineering, Peking University, Beijing 100871, China and [3]Chemistry Faculty, Lomonosov Moscow State University, Moscow 119991, Russia

***Corresponding authors.** E-mails: peiyunli@pku.edu.cn; zhizhang@pku.edu.cn; tinglei@pku.edu.cn

[†]Equally contributed to this work.

Received 24 March 2026; **Revised** 10 June 2026; **Accepted** 31 July 2026

INTRODUCTION

The demand for low power consumption and long-term stability has surged with the rise of wearable electronics, biosensors, and health monitoring systems [1]. Organic electrochemical transistors (OECTs) have emerged as a promising platform for low-power sensing applications, due to their low operating voltage, high transconductance (g_m), and outstanding biocompatibility [2,3]. Although OECTs inherently operate at relatively low voltages (<0.8 V) compared to other organic/inorganic transistors, they still need power consumption >100 nW to achieve satisfactory signal-to-noise (SNR) ratios for biosensing [4–6]. This poses great challenges for *in vivo* biosensing applications that are highly sensitive to heat generation, particularly for large-scale arrays or circuits [7–9]. The associated increase in power consumption and heat dissipation can accelerate organic material degradation and shorten device lifespan. Moreover, the long-term stability of OECT channel material, particularly n-type materials, remains a critical limitation that needs further improvement [10,11]. Therefore, reducing the power consumption of OECTs is critical to enabling their widespread adoption *in vivo*, low-power, long-lasting sensing applications.

N-type OECTs exhibit superior performance in biological sensing applications, particularly for enzyme-based sensing [12–15]. This is attributed to their ability to exhibit a progressive current increase in response to analyte interactions, which results in enhanced sensitivity to minor variations compared to p-type ones. The threshold voltage (V_{Th}), at which the OECT switches on, is crucial for assessing circuit power consumption and biosensor sensitivity, as it determines the operating voltage [16–18]. Ideally, a low V_{Th} is desirable to minimize power consumption and protect tissue from potential damage [16]. However, most reported high-performance n-type materials operate in enhancement mode (i.e. normally OFF)

© The Author(s) 2026. Published by Oxford University Press on behalf of China Science Publishing & Media Ltd. This is an Open Access article distributed under the terms of the Creative Commons Attribution License (https://creativecommons.org/licenses/by/4.0/), which permits unrestricted reuse, distribution, and reproduction in any medium, provided the original work is properly cited.

Downloaded from academic.oup.com/nsr/article/13/20/nwag489/8766035 by National Science & Technology Library user on 23 November 2026

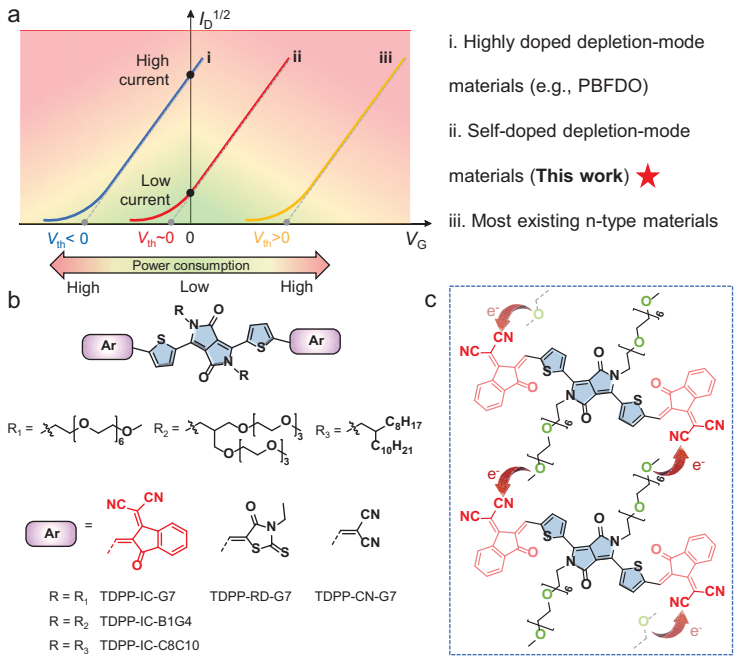


Figure 1. (a) Low-power-consumption design and V_{Th} comparisons of different n-type OECT materials. (b) Chemical structures of the self-doped molecules TDPP-IC-B1G4 and TDPP-IC-G7 and their non-self-doping counterparts TDPP-IC-C8C10, TDPP-CN-G7 and TDPP-RD-G7. (c) Schematic of the self-doping mechanism: electron transfer was found from its polar alkoxy side chain to the electron-deficient end group IC.

with V_{Th} generally exceeding 0.6 V (Fig. 1a-iii) [19–21]. While most integrated circuits are currently designed based on enhancement-mode transistors [6], depletion-mode OECTs have inherent advantages for long-term and real-time monitoring, as their channels are effectively doped (ON state) at zero gate bias. Operational stability also plays a critical role in ensuring long-term reliability and sensing accuracy. However, n-type depletion-mode materials are scarcely studied, and existing candidates entail trade-offs, including high turn-off voltage, low on/off ratio, or poor stability [19,22]. For example, the n-type depletion-mode material, PBFDO, has a V_{Th} largely below 0 V, and its highly doped state results in a low on/off ratio ($<10^2$), high power consumption due to high current, and very poor operating stability (Fig. 1a-i) [19,23]. Although chemical doping has been employed to tune the V_{Th} of n-type materials [24,25], the doping level is uncontrollable which can lead to instability in both materials and devices due to unpredictable dopant diffusion [26,27]. Therefore, how to design an n-type OECT material that can work in depletion mode with low V_{Th}, stable doping level, and good stability remains unsolved.

Here, we employed a self-doping strategy to achieve n-type OECTs with a controllable doping level, extremely low V_{Th}, and small currents at zero bias (Fig. 1a-ii). For the first time, we discovered that conventional ethylene glycol (EG) side chains could self-dope the conjugated backbone upon the introduction of certain functional groups. These self-doped molecules, TDPP-IC-B1G4 and TDPP-IC-G7, achieved an ultra-low V_{Th} below 0 V and a low operating voltage down to 0.05 V with excellent operational stability, outperforming their non-self-doped counterparts. When applied for biosensing, TDPP-IC-B1G4 exhibited exceptional biosensing performance with a high SNR and a power consumption as low as 12 nW, highlighting its considerable potential for highly stable and energy-efficient biosensing applications.

RESULTS AND DISCUSSION

Molecular design, synthesis and characterization

Thienyl diketopyrrolopyrrole (TDPP) was chosen as the building block due to its large π-conjugated backbone and strong intermolecular interactions [28–30]. 2-(3-oxo-2,3-dihydroinden-1-ylidene) malononitrile (IC) was chosen as the terminal functional group due to its strong electron-withdrawing ability, derived from its extended planar backbone and dual electron-deficient cyano groups. IC not only lowers the lowest unoccupied molecular orbital (LUMO) energy level but also facilitates intermolecular π–π stacking, thereby enhancing charge carrier mobility and ensuring stable n-doping in aqueous environments. Density functional theory (DFT) calculations revealed a low LUMO energy level of −3.92 eV for the TDPP-IC backbone (Fig. S1 and Table S1). The EG side chains were introduced to ensure good solubility and hydrophilicity of the molecules [31,32]. Linear oligomeric EG chains (G7) and branched oligomeric EG chains (B1G4) were introduced for comparison. The synthetic routes and detailed structural characterization of these two small molecules (TDPP-IC-B1G4 and TDPP-IC-G7) are shown in the Supporting Information. Furthermore, to investigate the relationship between molecular structure and self-doping behavior, we synthesized TDPP-IC with branched alkyl side chains (TDPP-IC-C8C10) [28] and TDPP with different end groups (TDPP-CN-G7 and TDPP-RD-G7) [33].

Side chains can influence molecules' aggregation and packing behaviors [34]. TDPP-IC-C8C10, TDPP-IC-G7, and TDPP-IC-B1G4 exhibited similar absorption profiles in dilute solution

Downloaded from academic.oup.com/nsr/article/13/20/nwag489/8766035 by National Science & Technology Library user on 23 November 2026

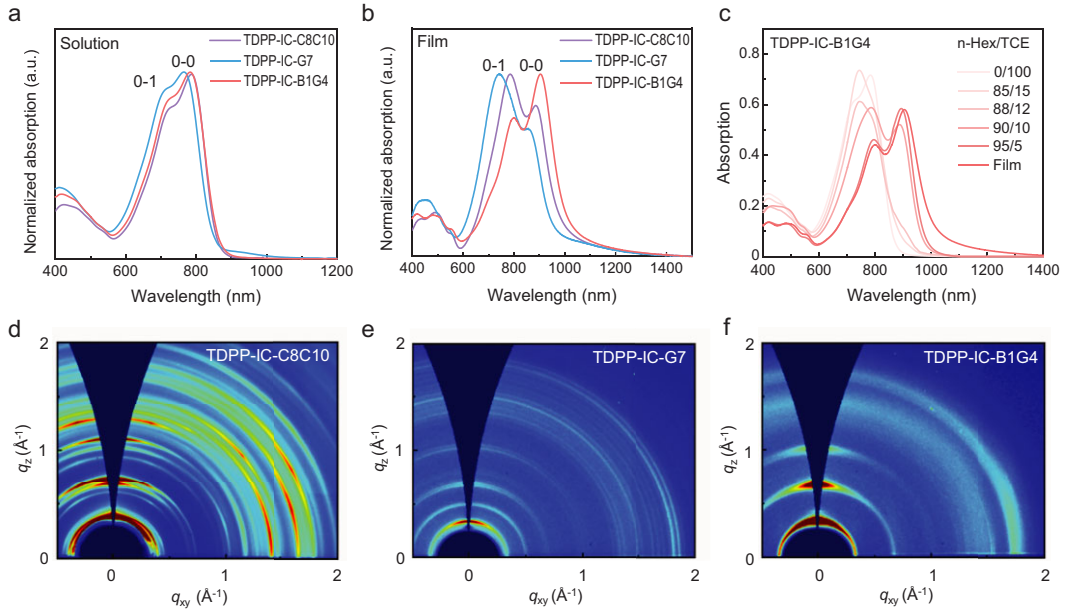


Figure 2. Molecular aggregation and packing behavior. (a and b) Normalized UV-vis-NIR absorption spectra of TDPP-IC-C8C10, TDPP-IC-G7, and TDPP-IC-B1G4 (a) in TCE solution (1×10^{-5} mol L^{-1}) and (b) in film. (c) Solvent-dependent absorption spectra of TDPP-IC-B1G4 in solution with different n-hexane/TCE volume ratios. (d–f) 2D GIWAXS patterns of spin-coated films for (d) TDPP-IC-C8C10, (e) TDPP-IC-G7 and (f) TDPP-IC-B1G4.

due to their same backbone (Fig. 2a). Interestingly, the three molecules exhibited distinct aggregation behaviors in thin-film states. TDPP-IC-B1G4 maintained J-type aggregation, whereas TDPP-IC-C8C10 and TDPP-IC-G7 underwent a transition to H-type aggregates upon film formation (Fig. 2b). To investigate the solution-state aggregation dynamics of TDPP-IC-B1G4, we measured the spectral evolution by adding poor solvent n-hexane into its tetrachloroethane (TCE) solution. Results indicated the J-type TDPP-IC-B1G4 aggregates sequentially transformed into H-type aggregates (85/15) and then into red-shifted J-type aggregates (95/5) (Fig. 2c). This finding is significant as it suggests different properties of the three small molecules, as our previous work demonstrated that J-aggregation can enhance the mobility of small molecules [33].

To further investigate the molecular packing and microstructures of the three molecules, grazing incidence wide-angle X-ray scattering (GIWAXS) measurements were conducted. TDPP-IC-C8C10 film exhibited polycrystalline diffraction patterns, consistent with typical small-molecule crystalline behavior (Fig. 2d) [33,35]. TDPP-IC-G7 film showed weaker but similar diffraction features (Fig. 2e). Notably, TDPP-IC-B1G4 film displayed distinct conjugated-polymer-like diffraction patterns with a preferential edge-on orientation (Fig. 2f), with a lamellar stacking distance (d_{lamellar}) of 18.5 Å and π–π stacking distance ($d_{\pi-\pi}$) of 3.67 Å (Fig. S2 and Table S2). The polymer-like molecular packing behavior arises from a unique supramolecular organization driven by a combination of J-type aggregation and strong intermolecular interactions [33]. Atomic force microscopy (AFM) measurements further indicated that the TDPP-IC-C8C10 film showed a polycrystalline and rough surface with a large root-mean-square (RMS) roughness of 10.4 nm, and TDPP-IC-G7 showed a reduced roughness of 6.29 nm. In contrast, the TDPP-IC-B1G4 film presented a smoother surface and nanofiber-like textures with a smaller RMS roughness of 2.29 nm (Fig. S3). We propose that the oriented edge-on packing, smaller RMS roughness, and J-type supramolecular self-assembly behavior of TDPP-IC-B1G4 may improve its intermolecular interactions, thereby facilitating higher carrier mobility and OECT performance [33,36].

OECT performance and low-power sensing

Spectroelectrochemistry was first performed to investigate the electrochemical characteristics of TDPP-IC-B1G4 in 0.1 M NaCl aqueous solution (Fig. 3a). As the applied bias varied from 0.2 to −0.3 V, the polaron absorption bands (950–1200 nm) increased while the neutral absorption bands (600–900 nm) decreased, demonstrating the

Downloaded from academic.oup.com/nsr/article/13/20/nwag489/8766035 by National Science & Technology Library user on 23 November 2026

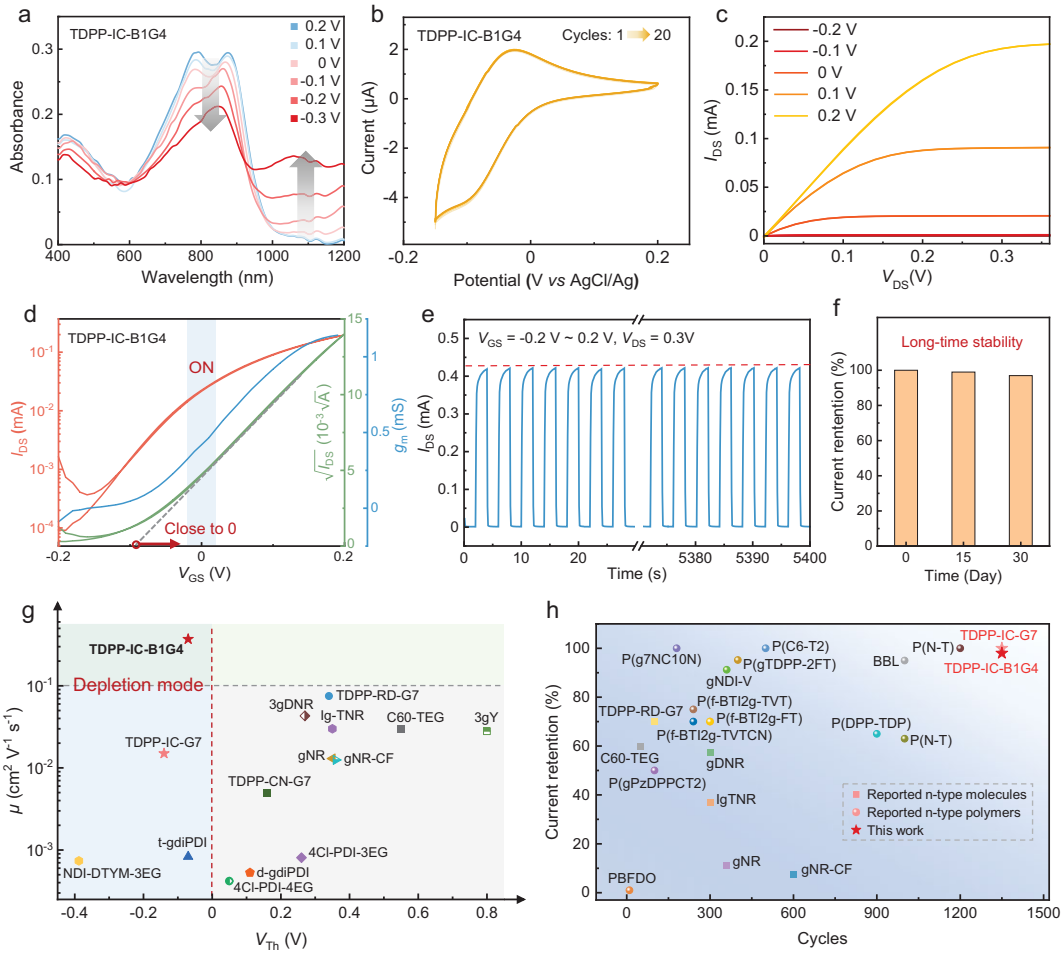


Figure 3. Electrochemical property and OECT performance of the self-doped molecules. (a) Electrochemical absorption spectra of TDPP-IC-B1G4 at different operating voltages in 0.1 M NaCl aqueous solution. (b) Continuous 20 cycles of cyclic voltammetry (CV) of TDPP-IC-B1G4 in 0.1 M NaCl aqueous solution. (c) Output characteristics of TDPP-IC-B1G4-based OECT. The OECT devices were measured in a 0.1 M NaCl aqueous solution and the gate electrode was an Ag/AgCl pellet. (d) Transfer characteristics of TDPP-IC-B1G4-based OECT (V_{DS} = 0.3 V, V_{GS} = −0.2 to 0.2 V, step = 10 mV). The blue line is the curve of g_m. (e) Operational stability of TDPP-IC-B1G4-based OECT device under 1350 on-off cycling measurements in air with V_{GS} applied as a square-wave pulse (−0.2 to 0.2 V, 4 s per pulse; Fig. S16,) and V_{DS} = 0.3 V, W/L = 1706.25, d = 13.5 nm. (f) Current retention of TDPP-IC-B1G4-based OECT (V_{DS} = 0.3 V, V_{GS} = 0.2 V) stored under ambient conditions without operation for 15 days and 30 days. (g) Comparison of the carrier mobility (μ) and V_{Th} for TDPP-IC-B1G4-based OECT device and other reported n-type small-molecule OECTs. (h) Comparison of the stability of TDPP-IC-B1G4 with other reported n-type OECT materials with the μC^* exceeding 1 F cm^{-1} V^{-1} s^{-1}.

electrochemical n-doping behavior of TDPP-IC-B1G4. Notably, TDPP-IC-B1G4 was electrochemically doped and conductive at a bias of 0 V, consistent with the established definition of depletion mode in semiconductor physics [37]. Electrochemical stability, another critical parameter for active materials, was evaluated through continuous cyclic voltammetry (CV) scans. The results showed that the CV curves of TDPP-IC-B1G4 film remained stable without any decay over 20 cycles, highlighting its high electrochemical stability (Fig. 3b). This is further supported by the repeated electrochemical absorption spectroscopy measurements (Fig. S4).

The OECT devices were fabricated by spin-coating the molecules' TCE solution onto a source-drain electrode-patterned substrate, followed by thermal annealing at 80°C for 10 min (see Supporting Information for more details). The OECT performance was evaluated using the Bernards' model [38]:

$$g_m = \frac{W d}{L} \mu C^* |V_{GS} - V_{Th}|, \quad (1)$$

Downloaded from academic.oup.com/nsr/article/13/20/nwag489/8766035 by National Science & Technology Library user on 23 November 2026

where μ is the charge carrier mobility, C^* is the volumetric capacitance, W, d, and L are the channel width, depth, and length, respectively.

Both self-doped small molecules exhibited typical n-type OECT behavior in the depletion mode (Fig. 3c and d, Figs S5 and S6), with the ultralow V_{Th} (−0.07 V for TDPP-IC-B1G4 and −0.14 V for TDPP-IC-G7, Tables S3 and S4 for more details and discussion) and low operating voltages (V_{DS} = 0.3 V). Since both molecules' LUMO are around −4.30 eV, higher than the reference AgCl/Ag electrode (−4.44 eV) (Fig. S7), their V_{Th} should be expected to be higher than zero if the molecules were in a neutral state. The observation of a negative V_{Th}, however, suggests that both molecules were already n-doped. The TDPP-IC-G7-based OECT showed a μC^* value of 0.12 F cm^{-1} V^{-1} s^{-1}, and the TDPP-IC-B1G4-based one exhibited a higher μC^* of 4.86 F cm^{-1} V^{-1} s^{-1}. To further understand the performance difference between the two molecules, C^* was measured using electrochemical impedance spectroscopy (EIS) at V_{GS} = 0.1 V. The average C^* values were 20.7 ± 11.5 F cm^{-3} for TDPP-IC-G7 and 22 ± 8.5 F cm^{-3} for TDPP-IC-B1G4 (Fig. S8). The calculated electron mobilities were 0.015 ± 0.004 cm^2 V^{-1} s^{-1} for TDPP-IC-G7 and 0.37 ± 0.15 cm^2 V^{-1} s^{-1} for TDPP-IC-B1G4, with the latter surpassing all reported n-type small molecules in the literature (Fig. 3g and Table S5) [21,33,35,39–43]. These results further demonstrate the positive effect of J-aggregation and molecular edge-on orientation on electron transport. Therefore, the superior OECT performance of TDPP-IC-B1G4 can be attributed to its high carrier mobility, which effectively offsets its relatively low C^*. Response time is also vital for sensing to enable real-time detection and rapid processing of dynamic changes [6,44]. To evaluate this performance, we tested the transient properties of OECT devices (Figs S5c and S6d). Response times were estimated by the exponential fitting of the I_{DS} curves. TDPP-IC-G7 exhibited response times with τ_{on} of 33.16 ms and τ_{off} of 6.5 ms, whereas TDPP-IC-B1G4 showed fast average response times with τ_{on} of 22.15 ms and τ_{off} of 13.42 ms, ranking among the fastest reported for small molecules (Table S6).

Long-term operational stability has been a persistent challenge that hinders the n-type OECT from practical applications [45]. Self-doping eliminates the need for dopant molecules, greatly improving the control over doping levels and presenting a promising strategy for enhancing material stability. As expected, both self-doped molecules showed excellent stability, matching well with electrochemical tests. Specifically, TDPP-IC-G7-based OECTs retained ∼107% and TDPP-IC-B1G4-based OECTs maintained ∼100% after 1.5 h of continuous operation (1350 on-off cycles) in aqueous solution in air (Fig. 3e and Figs S6c, S9, S17, S18). The stability surpasses that of all reported high-performance n-type OECT materials, establishing a record value (Fig. 3h). More importantly, TDPP-IC-B1G4-based OECTs maintained ∼97% of their initial current even after 1 month of air exposure (Fig. 3f). To our knowledge, such long-term stability has not been achieved before, despite its critical importance for practical applications. Overall, the TDPP-IC-B1G4 molecule combines ultra-low V_{Th}, high electrical performance, and outstanding stability (Fig. 3g and h), making it highly suitable for low-power sensing applications.

To demonstrate the capability of the molecules in low-power sensing, a bioelectrical signal sensor was constructed using the TDPP-IC-B1G4-based OECT and compared with a gold electrode of the same size. Human electrocardiogram (ECG) signals were recorded using the circuit illustrated in Fig. 4a. The human body was grounded to minimize signal interference (more details in the Supporting Information). The static power consumption (P_{static}) of an OECT-based sensor is defined in the following formula [5,46]:

$$P_{static} = V_{GS} \times I_{GS} + V_{DS} \times I_{DS}, \quad (2)$$

where the power consumption arises from both gate and drain consumptions. Although the transfer curve for a conventional large V_{Th} OECT can be shifted by changing the drain bias voltage to achieve low current [18], it always requires an extra gate voltage to switch the device ON and may generate non-negligible gate current leakage (I_{GS}), further compromising device stability and increasing power consumption. In contrast, the depletion mode of TDPP-IC-B1G4 enables its OECTs to operate at zero gate bias (V_{GS} = 0) (Fig. 4b), with negligible gate power consumption. By gradually decreasing the V_{DS} from 0.3 to 0.03 V, TDPP-IC-B1G4-based OECTs remained in the ON state and successfully captured the ECG signals (Fig. 4d). Detailed comparison results showed that while the SNR of the TDPP-IC-B1G4-based OECT devices decreased from ∼43 to 25 dB as the V_{DS} was reduced, it consistently remained higher than the SNR of the gold electrode. Additionally, the P_{static} of the TDPP-IC-B1G4-based OECTs decreased significantly from 100 nW at a

Downloaded from academic.oup.com/nsr/article/13/20/nwag489/8766035 by National Science & Technology Library user on 23 November 2026

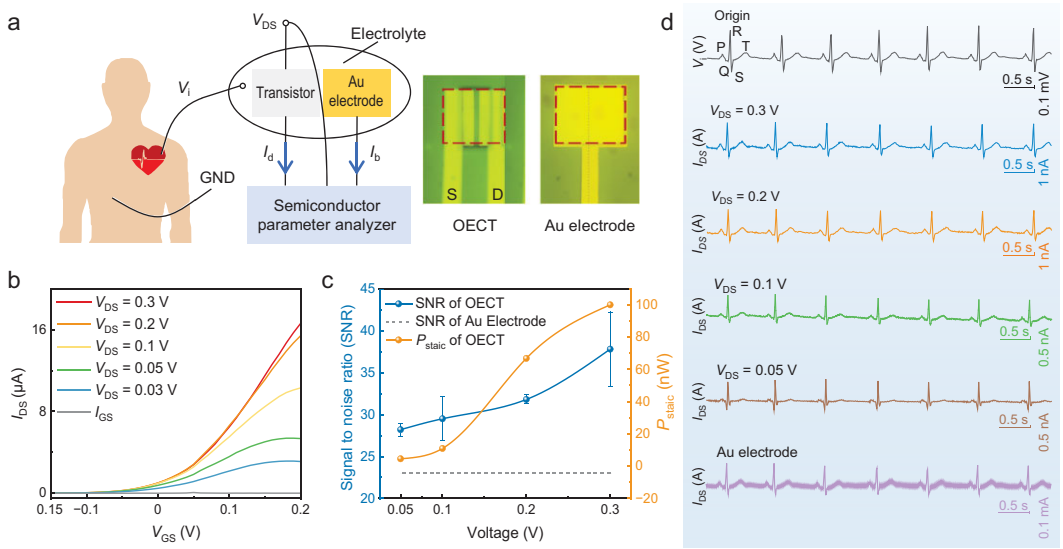


Figure 4. TDPP-IC-B1G4-based OECTs for low-power sensing. (a) Schematic of the electrocardiogram (ECG) measurement setup and microscope images of the gold electrode and the OECT devices with the same size. (b) Transfer curves of TDPP-IC-B1G4-based OECT devices with V_{DS} gradually decreasing from 0.3 to 0.03 V and V_{GS} varying from −0.15 to 0.2 V. (c) Signal-to-noise ratios (SNRs) of the ECG signals collected using gold electrodes and TDPP-IC-B1G4-based OECT devices, along with their static power consumption (P_{static}) under different V_{DS}. (d) ECG signals collected from the gold electrode and OECT devices as the V_{DS} voltage gradually decreased from 0.3 to 0.05 V, V_{GS} = 0 V.

V_{DS} of 0.3 V to just 12 nW at 0.05 V, achieving impressive SNRs at ultra-low power consumption (Fig. 4c and Table S7). In addition, n-type OECTs exhibit gradually increasing currents upon analyte interaction, offering potentially higher sensitivity in enzyme- [12] and analyte cations- [47] based sensing compared to p-type counterparts. To demonstrate, we developed enzyme-based sensors with good linear response, which can stably work at low operating voltage (Fig. S10). Compared to widely studied PEDOT: PSS, TDPP-IC-B1G4-based OECTs exhibit unique and critical advantages combining ultra-low power consumption, high sensitivity, and enhanced stability (Table S7 and discussion) [48,49], owing to their self-doping behavior that avoids instability from uncontrolled external dopants.

Self-doping mechanism

To gain deeper insights into the self-doping behavior, we conducted a series of characterizations on the small molecules with TDPP-IC backbones. Additionally, we included two previously reported molecules TDPP-RD-G7 and TDPP-CN-G7 [33], which have different end functional groups for comparison. Electron paramagnetic resonance (EPR) spectroscopy was employed to investigate their solid-state doping behavior. The EPR spectra showed that the TDPP-IC-B1G4 and TDPP-IC-G7 exhibited strong bimodal spin signals, indicating the presence of stable radicals, whereas TDPP-IC-C8C10, TDPP-RD-G7, and TDPP-CN-G7 showed no signal (Figs 5a and S11a). This distinction was further corroborated by electrical characterization. Top-gate/bottom-contact organic field-effect transistors (OFETs) based on TDPP-IC-C8C10, TDPP-RD-G7, and TDPP-CN-G7 exhibited n-type semiconducting characteristics (Figs 5b and S11b). In contrast, OFETs based on TDPP-IC-G7 and TDPP-IC-B1G4 remained constantly ON, signifying their pristine high carrier concentrations. Such high charge carrier concentrations were also confirmed by electrical conductivity and Hall effect measurements (Fig. S12 and Table S8). These results reveal that self-doping occurs only when both the IC end group and EG side chains are present simultaneously. To determine the carrier polarity, we measured the Seebeck coefficient, where its sign indicates the semiconductor's polarity. TDPP-IC-B1G4 displayed a Seebeck coefficient (S) of −588.15 μV K^{-1}, affirming that it is n-doped (Figs 5c and S13). Ultraviolet photoelectron spectroscopy further revealed that the secondary electron cut-off of the three IC molecule films shifted from 16.63 to 16.91 eV, corresponding to the Fermi level shift from −4.59 to −4.31 eV (Fig. 5d). Additionally, the onset of the highest occupied molecular orbital (HOMO) shifted to

Downloaded from academic.oup.com/nsr/article/13/20/nwag489/8766035 by National Science & Technology Library user on 23 November 2026

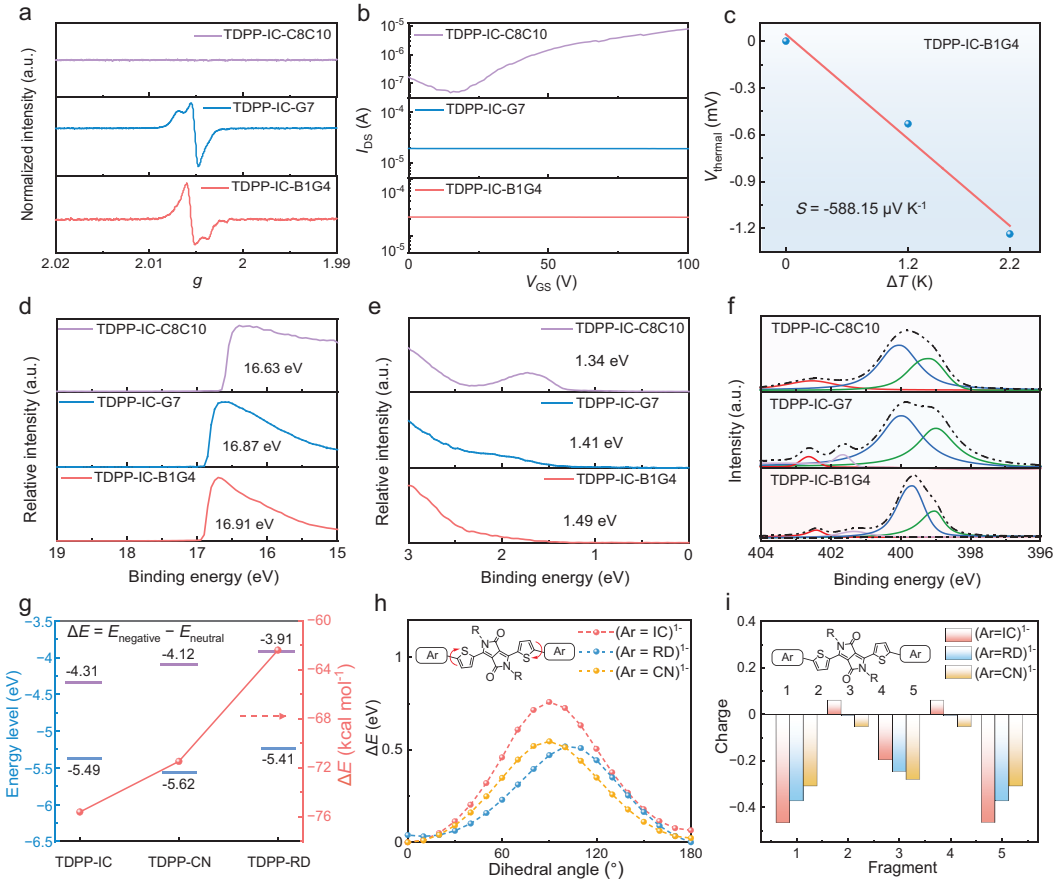


Figure 5. Self-doping characterization and mechanism analysis. (a) Electron paramagnetic resonance (EPR) spectra of the solid films of TDPP-IC-C8C10, TDPP-IC-G7, and TDPP-IC-B1G4. (b) Performance of top-gate/bottom-contact (TG/BC) OFETs fabricated using the three molecules. (c) Seebeck coefficient of TDPP-IC-B1G4. (d and e) Ultraviolet photoelectron spectroscopy spectra of the solid films of the three molecules. (f) X-ray Photoelectron Spectroscopy (XPS) spectra of the solid films of the three molecules. (g) Calculated energy difference between the neutral and negatively charged states of TDPP-IC-G7, TDPP-IC-CN, and TDPP-IC-RD. (h) Calculated torsional barriers of the three molecular backbones after electron acquisition. (i) Charge distribution of the three molecules after being negatively charged.

higher binding energies from 1.34 to 1.49 eV, corresponding to a HOMO level shift from −5.93 to −5.80 eV (Fig. 5e and Table S9). Considering that changes in molecular packing induced by side-chain variations do not significantly affect the density of states and the Fermi levels, we attributed the observed energy level changes to n-type doping. Therefore, the depletion-mode characteristics exhibited by TDPP-IC-G7 and TDPP-IC-B1G4 can be attributed to their side chain n-doping.

DFT calculations and X-ray photoelectron spectroscopy (XPS) were employed to identify the specific sites of n-doping. DFT-calculated electrostatic potential distribution of TDPP-IC indicates that the DPP core and the IC end groups are more positively charged (Fig. S14). To simulate the side chain doping, we respectively positioned two types of side chain fragments—a methoxy group ($C_2H_5OCH_3$) and an alkyl chain (C_4H_{10})—near the IC terminal group (rather than the TDPP core, considering steric hindrance due to molecular arrangement) with and without the existence of sodium ions and performed charge transfer calculations. The results indicated that the methoxy group, compared to alkyl side chains, exhibited a greater ability to transfer electrons to the TDPP-IC backbone. Moreover, the existence of sodium ions can enhance this electron transfer, which is facilitated by the hydrophilic EG chain. This result confirms that polar side chains can effectively dope the molecular backbone. Furthermore, XPS was used to characterize the chemical states of the sample films (Figs 5f and S11c). The N 1s XPS spectrum of TDPP-IC-C8C10 revealed three main peaks: those at 399.18 and 400.08 eV

Downloaded from academic.oup.com/nsr/article/13/20/nwag489/8766035 by National Science & Technology Library user on 23 November 2026

correspond to the C—N $(C)_2$ and —N—(C=O) groups in the DPP backbone; the peak at 402.53 eV is attributed to the —C≡N group in the end group. Most peaks of TDPP-IC-G7 and TDPP-IC-B1G4 matched those in TDPP-IC-C8C10, confirming the presence of the same DPP backbone and end group. A new peak around 401–402 eV indicates the possible formation of a radical anion $(-C{\equiv}N)^{-\bullet}$, suggesting electron transfer from the polar side chain to the end CN group. These results suggest that the alkoxy side chains can effectively dope the molecular backbone, potentially via charge transfer interactions between the alkoxy chains and the end functional groups. The absence of self-doping peaks in the XPS profiles of TDPP-CN-G7 and TDPP-RD-G7 further confirms the self-doping mechanism (Fig. S11c).

To further understand the doping mechanism, DFT calculations, and CV measurements were performed on the three molecules with different end groups (TDPP-IC-G7, TDPP-CN-G7, and TDPP-RD-G7). CV measurements revealed the lowest LUMO of TDPP-IC-G7 among the three molecules (Fig. 5g, Table S1, and Fig. S15). The deeper LUMO level of TDPP-IC-G7 makes it more likely to accept electrons from the polar side groups, indicating stronger doping behavior. We calculated the energy difference between the neutral and negatively charged state ΔE ($E_{\text{negative}} - E_{\text{neutral}}$). TDPP-IC-G7 showed the lowest ΔE of −75.6 kcal mol^{-1}, compared to −62.4 kcal mol^{-1} for TDPP-RD-G7 and −71.4 kcal mol^{-1} for TDPP-CN-G7 (Fig. 5g). This suggests that the negative polarons on the TDPP-IC-G7 backbone are more stable. The torsional barrier of these three molecules in negatively charged states is calculated (Fig. 5h). TDPP-IC-G7 also exhibited the largest torsional barrier, demonstrating its more rigid backbone after n-doping, which could benefit charge transport under n-doped states. Additionally, the charge distribution after adding one electron to the backbone reveals that the IC end group can share more negative charges than RD and CN (Fig. 5i). Therefore, the IC end group possesses a strong electron acquisition capability and can effectively stabilize the polaron, leading to enhanced polaron transport. Based on the above analysis, the self-doping is driven by the electron transfer from the polar EG side chains to the IC end groups.

CONCLUSION

In summary, we discovered the self-n-doping ability of alkoxy side chains and developed self-doped OECT materials TDPP-IC-G7 and TDPP-IC-B1G4. TDPP-IC-B1G4 exhibited J-type polymer-like edge-on packing, which likely contributes to its enhanced charge-transport properties. As a result, TDPP-IC-B1G4 demonstrated a high electron mobility (0.37 ± 0.15 cm^2 V^{-1} s^{-1}), low V_{Th} (−0.07 V), ultra-low operating voltage (down to 0.05 V), and exceptional operational stability. Operating in depletion mode, TDPP-IC-B1G4-based OECT is well-suited for biosensors, exhibiting high SNR ratios and ultra-low power consumption (12 nW). Through systematic characterization and computational analysis, we demonstrated that the self-doping mechanism of alkoxy chains is driven by the inherently high electron affinity of the backbone and the formation of stable negative polarons. Looking forward, the self-n-doping strategy established herein can be extended to other molecular backbones, potentially expanding the library of high-performance n-type OECT materials. More importantly, low-operation-voltage n-type OECT materials are scarce, resulting in high operational voltages for both complementary circuits and biosensors. We believe our findings will accelerate the discovery of low-voltage, low-power-consumption circuits and biosensors, which are critical for biointerfacing electronics.

SUPPLEMENTARY DATA

Supplementary data are available at *NSR* online.

ACKNOWLEDGEMENTS

We acknowledge the Molecular Materials and Nanofabrication Laboratory (MMNL) and the Materials Processing and Analysis Center, Peking University, for the use of instruments. The computational part was supported by the High-Performance Computing Platform of Peking University.

FUNDING

This work was supported by Beijing Natural Science Foundation (F261024 and 2262050), the National Natural Science Foundation of China (52403219, T2425010 and T2521001), the Fundamental Research Funds for the Central Universities, Peking University (PKU2026PKULCXQ023), and the Excellent Young Scientific and Technological Talents Project of Zhengzhou (2025QNKJ048).

AUTHOR CONTRIBUTIONS

K.-K.L., X.L. and G.G. synthesized the small molecules and performed some material characterization. Y.L. and P.L. performed device fabrication and characterization. X.L. and Y.L. performed DFT calculations. J.W. performed Seebeck measurements. X.L. and J.W. performed the AC-Hall test. X.-Y.D. performed the EPR measurement. X.L., Y.L. and Z.Z.

Downloaded from academic.oup.com/nsr/article/13/20/nwag489/8766035 by National Science & Technology Library user on 23 November 2026

performed data analysis and processing. X.L., Y.L., P.L., M.K., Z.Z. and T.L. wrote the manuscript. All the authors revised and approved the manuscript.

Conflict of interest statement. None declared.

REFERENCES

1. Zhu Z, Pang Y, Li Y *et al.* The rising of flexible organic electrochemical transistors in sensors and intelligent circuits. *ACS Nano* 2025; **19**: 4084–120.
2. Rivnay J, Inal S, Salleo A *et al.* Organic electrochemical transistors. *Nat Rev Mater* 2018; **3**: 17086.
3. Wu J, Liu H, Chen W *et al.* Device integration of electrochemical biosensors. *Nat Rev Bioeng* 2023; **1**: 346–60.
4. Zhao C, Yang J, Ma W. Transient response and ionic dynamics in organic electrochemical transistors. *Nano-Micro Lett* 2024; **16**: 233.
5. Zhou Z, Wu X, Tam TLD *et al.* Highly stable ladder-type conjugated polymer based organic electrochemical transistors for low power and signal processing-free surface electromyogram triggered robotic hand control. *Adv Funct Mater* 2023; **34**: 2305780.
6. Cea C, Spyropoulos GD, Jastrzebska-Perfect P *et al.* Enhancement-mode ion-based transistor as a comprehensive interface and real-time processing unit for in vivo electrophysiology. *Nat Mater* 2020; **19**: 679–86.
7. Cea C, Zhao Z, Wisniewski DJ *et al.* Integrated internal ion-gated organic electrochemical transistors for stand-alone conformable bioelectronics. *Nat Mater* 2023; **22**: 1227–35.
8. Liu D, Tian X, Bai J *et al.* A wearable in-sensor computing platform based on stretchable organic electrochemical transistors. *Nat Electron* 2024; **7**: 1176–85.
9. Kim J, Pankow RM, Cho Y *et al.* Monolithically integrated high-density vertical organic electrochemical transistor arrays and complementary circuits. *Nat Electron* 2024; **7**: 234–43.
10. Giovannitti A, Nielsen CB, Sbircea D-T *et al.* N-type organic electrochemical transistors with stability in water. *Nat Commun* 2016; **7**: 13066.
11. Paterson AF, Savva A, Wustoni S *et al.* Water stable molecular n-doping produces organic electrochemical transistors with high transconductance and record stability. *Nat Commun* 2020; **11**: 3304.
12. Pappa AM, Ohayon D, Giovannitti A *et al.* Direct metabolite detection with an n-type accumulation mode organic electrochemical transistor. *Sci Adv* 2018; **4**: eaat0911.
13. Huang W, Chen J, Yao Y *et al.* Vertical organic electrochemical transistors for complementary circuits. *Nature* 2023; **613**: 496–502.
14. Ohayon D, Nikiforidis G, Savva A *et al.* Biofuel powered glucose detection in bodily fluids with an n-type conjugated polymer. *Nat Mater* 2019; **19**: 456–63.
15. Wu W, Feng K, Wang Y *et al.* Selenophene substitution enabled high-performance n-type polymeric mixed ionic-electronic conductors for organic electrochemical transistors and glucose sensors. *Adv Mater* 2024; **36**: 2310503.
16. Tan STM, Lee G, Denti I *et al.* Tuning organic electrochemical transistor threshold voltage using chemically doped polymer gates. *Adv Mater* 2022; **34**: 2202359.
17. Ding R, Zhang X, Yan R *et al.* Ultra-low threshold voltage in n-type organic electrochemical transistors enabled by organic mixed ionic-electronic conductors with dual electron-withdrawing substitutions. *Adv Funct Mater* 2024; **35**: 2412181.
18. Doris SE, Pierre A, Street RA. Dynamic and tunable threshold voltage in organic electrochemical transistors. *Adv Mater* 2018; **30**: 1706757.
19. Tang H, Liang Y, Liu C *et al.* A solution-processed n-type conducting polymer with ultrahigh conductivity. *Nature* 2022; **611**: 271–7.
20. Feng K, Shan W, Ma S *et al.* Fused bithiophene imide dimer-based n-type polymers for high-performance organic electrochemical transistors. *Angew Chem Int Ed* 2021; **60**: 24198–205.
21. Duan J, Zhu G, Chen J *et al.* Highly efficient mixed conduction in a fused oligomer n-type organic semiconductor enabled by 3D transport pathways. *Adv Mater* 2023; **35**: 2300252.
22. Liu X, Xiao Y, Yan C *et al.* Structural modifications for tuning performance and operational modes in n-type organic electrochemical transistors. *ACS Appl Mater Interfaces* 2025; **17**: 8072–83.
23. Wu X, Tang H, Zhou Z *et al.* Improved stability and performance of an n-type depletion mode poly(benzodifurandione) based organic electrochemical transistor via electrolyte selection. *Chem Mater* 2024; **36**: 8639–48.
24. Yang C-Y, Stoeckel M-A, Ruoko T-P *et al.* A high-conductivity n -type polymeric ink for printed electronics. *Nat Commun* 2021; **12**: 2354.
25. Tang H, Xu Z, Liang Y *et al.* Highly conductive alcohol-processable n-type conducting polymer enabled by finely tuned electrostatic interactions for green organic electronics. *Angew Chem Int Ed* 2024; **64**: e202415349.
26. Xu Y, Sun H, Liu A *et al.* Doping: a key enabler for organic transistors. *Adv Mater* 2019; **30**: 1801830.
27. Qin M, Zeng Z, Ma F *et al.* Doping in solvation structure: enabling fluorinated carbonate electrolyte for high-voltage and high-safety lithium-ion batteries. *ACS Energy Lett* 2024; **9**: 2536–44.
28. Ge GY, Li JT, Wang JR *et al.* Unveiling the interplay among end group, molecular packing, doping level, and charge transport in n-doped small-molecule organic semiconductors. *Adv Funct Mater* 2022; **32**: 2108289.
29. Li P, Shi J, Lei Y *et al.* Switching p-type to high-performance n-type organic electrochemical transistors via doped state engineering. *Nat Commun* 2022; **13**: 5970.
30. Yang J, Zhao Z, Wang S *et al.* Insight into high-performance conjugated polymers for organic field-effect transistors. *Chem* 2018; **4**: 2748–85.

Downloaded from academic.oup.com/nsr/article/13/20/nwag489/8766035 by National Science & Technology Library user on 23 November 2026

31. Lei T, Wang J-Y, Pei J. Roles of flexible chains in organic semiconducting materials. *Chem Mater* 2013; **26**: 594–603.
32. Wang XY, Liu Y, Wang ZY *et al.* Revealing the effect of oligo(ethylene glycol) side chains on n-doping process in FBDPPV-based polymers. *J Polym Sci* 2021; **60**: 538–47.
33. Liu KK, Li P, Lei Y *et al.* J-type self-assembled supramolecular polymers for high-performance and fast-response n-type organic electrochemical transistors. *Adv Funct Mater* 2023; **33**: 2300049.
34. Xu J, Wu H-C, Mun J *et al.* Tuning conjugated polymer chain packing for stretchable semiconductors. *Adv Mater* 2021; **34**: 2104747.
35. Zhu G, Chen J, Duan J *et al.* Fluorinated alcohol-processed n-type organic electrochemical transistor with high performance and enhanced stability. *ACS Appl Mater Interfaces* 2022; **14**: 43586—96.
36. Chen S, Zhu S, Lin Z *et al.* Transforming polymorphs via meniscus-assisted solution-shearing conjugated polymers for organic field-effect transistors. *ACS Nano* 2022; **16**: 11194—203.
37. Sze SM and Ng KK. MOSFETs. In: *Physics of Semiconductor Devices*. Hoboken: John Wiley & Sons, 2006, 296–7.
38. Bernards DA and Malliaras GG. Steady-state and transient behavior of organic electrochemical transistors. *Adv Funct Mater* 2007; **17**: 3538–44.
39. Bischak CG, Flagg LQ, Yan K *et al.* Fullerene active layers for n-type organic electrochemical transistors. *ACS Appl Mater Interfaces* 2019; **11**: 28138—44.
40. Duan J, Zhu G, Wang L *et al.* Highly efficient mixed conduction in n-type fused small molecule semiconductors. *Adv Funct Mater* 2022; **32**: 2203937.
41. Duan J, Zhu G, Lan L *et al.* Electron-deficient polycyclic molecules via ring fusion for n-type organic electrochemical transistors. *Angew Chem Int Ed* 2023; **62**: e202213737.
42. Liao H, Chen J, Lan L *et al.* Efficient n-type small-molecule mixed ion-electron conductors and application in hydrogen peroxide sensors. *ACS Appl Mater Interfaces* 2022; **14**: 16477—16486.
43. Yu Y, Zhu G, Lan L *et al.* N-type glycolated imide-fused polycyclic aromatic hydrocarbons with high capacity for liquid/solid-electrolyte-based electrochemical devices. *Adv Funct Mater* 2023; **33**: 2300012.
44. Rivnay J, Leleux P, Ferro M *et al.* High-performance transistors for bioelectronics through tuning of channel thickness. *Sci Adv* 2015; **1**: e1400251.
45. Lei Y, Li P, Zheng Y *et al.* Materials design and applications of n-type and ambipolar organic electrochemical transistors. *Mater Chem Front* 2023; **8**: 133–58.
46. Wang X, Meng X, Zhu Y *et al.* A sub-1-V, microwatt power-consumption iontronic pressure sensor based on organic electrochemical transistors. *IEEE Electron Device Lett* 2021; **42**: 46–9.
47. Huang W, Chen JH, Yao Y *et al.* Vertical organic electrochemical transistors for complementary circuits. *Nature* 2023; **613**: 496–502.
48. Tang K, Miao WJ, Guo S. Crosslinked PEDOT:PSS organic electrochemical transistors on interdigitated electrodes with improved stability. *ACS Appl Polym Mater* 2021; **3**: 1436–44.
49. Xie M, Liu HF, Wu MG *et al.* Cycling stability of organic electrochemical transistors. *Org Electron* 2023; **117**: 106777.

Downloaded from academic.oup.com/nsr/article/13/20/nwag489/8766035 by National Science & Technology Library user on 23 November 2026

© The Author(s) 2026. Published by Oxford University Press on behalf of China Science Publishing & Media Ltd. This is an Open Access article distributed under the terms of the Creative Commons Attribution License (https://creativecommons.org/licenses/by/4.0/), which permits unrestricted reuse, distribution, and reproduction in any medium, provided the original work is properly cited.